Ultrasonic specific absorption rate in nanoparticle-mediated moderate hyperthermia

Barbara GAMBIN[*] and Eleonora KRUGLENKO

Institute of Fundamental Technological Research, Polish Academy of Sciences, ul. Pawińskiego 5B, 02-106 Warsaw, Poland

Abstract. Magnetic nanoparticle's different applications in nanomedicine, due to their unique physical properties and biocompatibility, were intensively investigated. Recently, Fe_3O_4 nanoparticles, are confirmed to be the best sonosensitizers to enhance the performance of HIFU (high intensity focused ultrasound). They are also used as thermo-sensitizers in magnetic hyperthermia. A new idea of dual, magneto-ultrasound, coupled hyperthermia allows the ultrasound intensity to be reduced from the high to a moderate level. Our goal is to evaluate the enhancement of thermal effects of focused ultrasound of moderate intensity due to the presence of nanoparticles. We combine experimental results with numerical analysis. Experiments are performed on tissue-mimicking materials made of the 5% agar gel and gel samples containing Fe_3O_4 nanoparticles with $\phi = 100$ nm with two fractions of 0.76 and 1.53% w/w. Thermocouples registered curves of temperature rising during heating by focused ultrasound transducer with acoustic powers of the range from 1 to 4 W. The theoretical model of ultrasound-thermal coupling is solved in COMSOL Multiphysics. We compared the changes between the specific absorption rates (SAR) coefficients determined from the experimental and numerical temperature rise curves depending on the nanoparticle fractions and applied acoustic powers. We confirmed that the significant role of nanoparticles in enhancing the thermal effect is qualitatively similarly estimated, based on experimental and numerical results. So that we demonstrated the usefulness of the FEM linear acoustic model in the planning of efficiency of nanoparticle-mediated moderate hyperthermia.

Key words: ultrasonic hyperthermia; agar-based tissue mimicking phantom; magnetic nanoparticles; temperature; specific absorption rate (SAR).

1. Introduction

Hyperthermia is the therapy of the temperature increment of the human body to care for different kinds of illnesses. Temperature increases inside the body can be activated by ultrasound or alternating magnetic field, namely ultrasonic or magnetic hyperthermia. The basics of temperature rise effects on living cells and cell internal molecular structure were explained in [1–3], and more recently in [4]. It was already proved that temperature increase over the body temperature level initiates the production of Heat Shock Proteins (HSP) and cell signaling pathways, which are essential for intracellular protein folding during stress, see e.g., [5]. It can protect cells from denaturation and aggregation cascades that can lead to cell death. If the temperature increase is not very high, this is mild or moderate hyperthermia, see [6]. The ultrasonic mild hyperthermia effect on the cellular reaction was studied e.g., in [7–9] and references therein. The hyperthermia which is induced with very high-intensity ultrasound, in which the targeted tissue area is destroyed in a short time, is a HIFU (High-Intensity Focused Ultrasound) treatment. Comparatively new hyperthermia, including the HIFU technique, namely nanoparticle-mediated hyperthermia, in which nanoparticles added to tissue play a crucial role in the localization and the therapy acceleration, is currently investigated in various aspects of nanomedicine, see

e.g., [10, 11] and book [12]. Many different nanoparticles for hyperthermia applications are currently being studied, nanoparticles of gold, silver, iron oxide, etc., cf. [13–15], and references therein. However, it has been noticed that Fe_3O_4 nanoparticles exhibit a higher thermal effect than gold nanoparticles in ultrasonic hyperthermia [14]. Effective and least interventional cancer destruction is one of the main goals of nanoparticle-mediated hyperthermia, see [16]. It still raises great hopes to fight cancer cf. the review paper [17], book [18]. The usefulness of magnetic nanoparticles due to their unique properties is stated in preliminary studies of new bi-modal hyperthermia, coupling the thermal effects of ultrasound, and an alternating magnetic field. The nanoparticle-mediated "pure" magnetic hyperthermia has been extensively studied in the last decade, see e.g., [19]. In that paper, the author combined experimental results of heating measurements with numerical analysis in order to calibrate the model used for planning therapy *in vivo*. We will use a similar procedure for our work. Preliminary studies of the bi-modal, ultrasonic-magnetic, hyperthermia have yielded promising results e.g., [20–22], and recently [23]. Thanks to the simultaneous action of both fields, ultrasonic and magnetic, in magnetic nanoparticle-mediated bi-modal hyperthermia, we expect to obtain enough strong thermal effects under the application of lower acoustic power than in HIFU. In this case, we also eliminate the appearance of unfavorable cavitation that normally accompanies HIFU sonication. This is our main motivation for researching the effects of magnetic nanoparticles on the enhancement of moderate hyperthermia, which is presented below in this paper. HIFU useful in hyperthermia is updated problem, studied extensively, see e.g., [24] and [25]. In

B. Gambin and E. Kruglenko

this research paper we focused on moderate hyperthermia also because the strong and fast heating processes in HIFU are more difficult to study from both the measurement and explanation of physical phenomena occurring in them. Many new problems appear due to coupled phenomena like heat dissipation in high temperatures can change the diffusional character of heat conduction in the presence of nanoparticles, a non-equilibrium thermodynamic can worry, also wave processes lose their linear character, etc. Contrary, this paper deals with the thermal effects in tissue with magnetic nanoparticles appearing under moderate-intensity focused ultrasound.

The purpose of this article is to evaluate the usefulness of adding magnetic nanoparticles to tissues to enhance moderate ultrasonic hyperthermia. To achieve this goal, differences in the course of the ultrasonic beam heating process of tissue without nanoparticles and with embedded nanoparticles are compared. For reasons of repeatability and monitoring of the temperature increase process, experiments have been carried out on agar-based self-fabricated tissue-mimicking materials (TMMs), see [26]. The value of ultrasonic absorption is the key parameter in the assessment of hyperthermia. The nature of the temperature rise, or more precisely the initial temperature rise during the heating process, is used to determine the experimentally specific absorption rate (SAR). Using the assumption of the diffusive nature of heat transport in tissues, the SAR value is proportional to the initial temperature change rate. It should be underlined that monitoring of the heating process of TMMs containing magnetic nanoparticles cannot be carried out by MRI (magnetic resonance imaging) thermometry as it is possible when monitoring the temperature rise in TMMs with organic or more generally non-magnetic nanoparticles, see [27]. Unfortunately, the presence of magnetic nanoparticles disturbs proton magnetic susceptibility, see [12]. Therefore, only thermocouples that record temperature locally are used to study temperature changes at TMMs with magnetic nanoparticles. The use of thermocouples or other thermometers with sensors embedded inside the heated area is interventional and therefore out of the question for *in vivo* tissue testing. Therefore, the prediction of the influence of the presence of nanoparticles in tissue on the enhancement of the effect of hyperthermia *in vivo* can only be performed *in silico*, i.e., based on numerical modeling.

In what follows, we propose a hybrid method combining experimental measurement with theoretical and numerical analysis to determine the differences in thermal effects of ultrasound of moderate acoustic power irradiation between tissue with and without magnetic nanoparticles. We perform the heating experiments on tissue-mimicking materials made of the pure agar gel and agar-gel with the addition of magnetic nanoparticles with a diameter of 100 nm diameter with two fractions, 0.76 and 1.53% w/w. The theoretical model of ultrasound thermal effects due to nanoparticle presence is numerically solved in COMSOL Multiphysics. The linear acoustic model is used in numerical simulations of heat source generation caused by ultrasonic beam formation. We compare the curves of temperature rising measured during the heating of samples by focused ultrasound transducer with different acoustic powers with numerical simulations. The differences and similarities are discussed

in the dependence on thermal parameters used in simulations and the time duration of heating. As a measure of the influence of nanoparticle presence on hyperthermia enhancement, the relative changes in specific absorption rates (SAR) in tissue with and without nanoparticles, driven from experiments and simulations, are used. The usefulness of the numerical simulations for *in vivo* hyperthermia study is discussed.

2. Materials and methods

2.1. TMM agar-based samples. Procedures of samples preparation together with materials used in them, also thermal heating experiments performed were analogous to these was described in detail in [26], and [28]. The dedicated hyperthermia experimental setup described in these papers was specially designed with thermocouple guides to locate them precisely on the beam axis, cf. [29]. Fe_3O_4 nanoparticles with $\phi = 100$ nm (Sigma-Aldrich, Germany), and agar in the form of pure agarose (Agarose BIO STANDARD, Prona) were used. Note that the preparation of an agar gel containing nanoparticles required an aqueous suspension of nanoparticles. As the suspension was unstable, agar powder was added while sonicating the suspension to increase stability. The homogeneity of the obtained structure in mm scale was assessed from SEM images of the frozen samples, see Fig. 1. It should be also noted that the homogeneity of agar samples can be achieved in a simpler way by using ferrofluids for agar gelation. Many studies have been devoted to the physical properties of various ferrofluids, which are stable iron-containing suspensions prepared for medical purposes, e.g., [30, 31]. We showed that the physical and acoustic properties qualify agar-gel samples with nanoparticles as tissue-mimicking materials (TMMs) useful for testing ultrasonic hyperthermia, [26]. Three types of samples were prepared. The first type of sample was made of the pure 5% agarose gel, and two other were made of this gel with the addition of nanoparticles in two different proportions of 8 and 16 mg/ml. The weight fractions of nanoparticles for these two types of samples are 0.76 and 1.53% w/w, respectively. In what follows we use abbreviated names for these two samples with nanoparticles, MNP8 and MNP16, depending on particle fraction, respectively, cf. [26, 28]. In Fig. 1 Scanning Electron Microscope (SEM) images of dry powder of nanoparticles and a
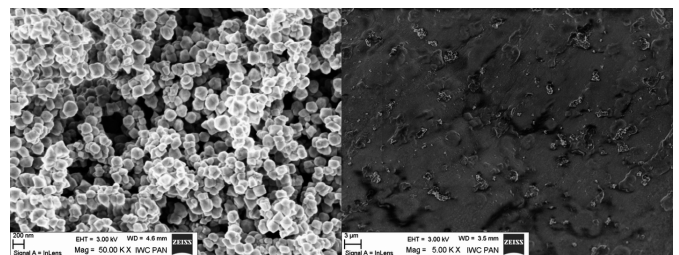

Fig. 1. Scanning Electron Microscope (SEM) images of nanoparticles Fe_3O_4 powder with a dimension of 100 nm on the left, and of a frozen agar-based sample NMP16 on the right. Images obtained by courtesy of Mrs. Makarowa I. from the Institute of High Pressure, Polish Academy of Sciences

frozen agar-gel sample with embedded nanoparticles, NMP16, are presented.

The measurement of the acoustic properties of the samples was described in [26], the values of attenuation and speed of sound are repeated in Table 1 because these data are used in numerical modeling.

Table 1
Material properties

Sample	Density kg/m^3	Attenuation dB/(MHz·cm)	Specific heat J/(kg·K)	Conductivity W/(m·K)
Water	1000	0.002	4200	0.60
Agar	1011	0.025	4200	0.55
MNP8	1020	0.21	4176	0.55
MNP16	1032	0.66	4172	0.55

Thermal conductivity of gel with different agarose concentrations in the temperature range from 5°C to 50°C was reported in [32]. For an agar with a 0.05 (5%) agar weight fraction, the thermal conductivity increases with temperature and was in the range 0.55–0.62 [W/(m·K)]. Fe_3O_4 thermal conductivity was equal to 5.3 [W/(m·K)], and the thermal conductivities of MNP8 and MNP16 were calculated from mixture principles like in [33] The volume fractions of nanoparticles in the samples MNP8 and MNP16 are 0.154 and 0.307% v/v, respectively, calculated under the assumption that they are spheres with 100 nm diameters. The thermal properties of considered samples are listed in Table 1.

2.2. Temperature monitoring during sonication. The system for measuring the temperature caused by the ultrasonic wave has been described in detail in [34,35]. Below, we repeat a brief description. The sample was immersed in a container with water at a constant temperature of 25°C. The temperature rise was measured by using 7 of K-type thermocouples (NiCr-NiAl, $\phi = 0.5$ mm, accuracy = ±0.5°C, resolution = 0.1°C, Czaki Thermo-Product. Poland) which were placed inside the sample along the beam axis, at mutual distances of 5 mm. The thermocouple sensors were positioned perpendicular to the axis of the ultrasonic beam in order to minimize the artifact of reading the temperature rise associated with direct exposure of the thermocouples and, thus, viscous heating artifacts, cf. [36]. Four thermocouples were placed in the sample between the focus and transducer, and two behind the focus. The temperature curves were monitoring during the 300 s of heating and 300 s of cooling and registered on a USB-TEMP temperature meter (Measurement Computing Corporation, Norton, USA) with a frequency of 1 per sec. The ultrasonic circular, focused transducer (Meggitt, Kvistgaard, Denmark) with a diameter of 44 mm, a focal length of 44 mm, and operating at a frequency of 2.2 MHz was used. The ultrasound beam was broadcast 20-cycle tone bursts with a duty-cycle of 0.2 and a pulse duration of 45 ms. The electronic transmitter system, see Fig. 2, consisted of a generator (Agilent 33250A, Colorado Springs, USA), a power amplifier (ENI 3100LA Rochester, NY, USA), and an oscilloscope
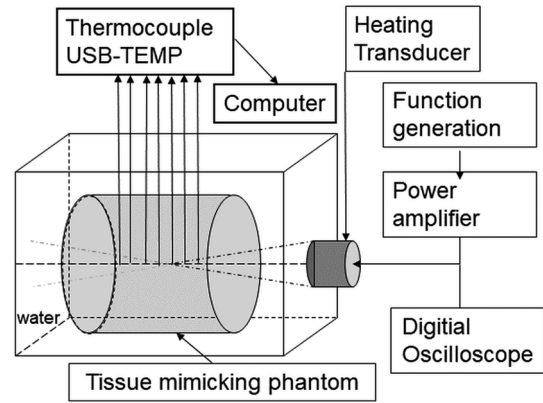

Fig. 2. Scheme of the experimental setup of ultrasound heating of the sample with the marked location of thermocouples

(Tektronix TDS3012B Beaverton, USA). The experiment was conducted for four values of sound power radiated by the transducer; 1, 2, 3, and 4 watts measured using the ultrasound power meter (model UPM-DT-1&10, Ohmic Instruments Inc., USA).

The average radiated acoustic beam power was measured by an ultrasound power meter (UPM-DT-1 E, Ohmic Instruments Co, Easton, USA). The location and shape of the beam were experimentally identified, by thoroughly measuring the pressure distribution in water with a needle hydrophone (PA 0.2 mm).

2.3. Theory

2.3.1. Bioheat transfer. In what follows, we use bold fonts, upper case or lower case, to denote tensors, vectors, and plain fonts for scalars (or when using indicial notation). The Pennes' bioheat transfer equation in an inhomogeneous thermally anisotropic medium, occupying the domain V in the 3D space, see [37], has the form:

$$\rho(\mathbf{x})C(\mathbf{x})\frac{\partial T(\mathbf{x},t)}{\partial t} = \boldsymbol{\nabla} \cdot \mathbf{K}(\mathbf{x}) \cdot \boldsymbol{\nabla} T(\mathbf{x},t) + Q_p(\mathbf{x},t)$$
$$+ Q_{met}(\mathbf{x},t) + Q(\mathbf{x},t), \quad \text{for } \mathbf{x} \in V, \quad (1)$$

where $(\cdot)$ denotes tensor contraction, $\rho, C, \mathbf{K}$ denote the density, specific heat and thermal conductivity of a medium (tensor of order 2), respectively, $\boldsymbol{\nabla}$ is a gradient operator, and Q_p, Q_{met} are heat sources densities generated by blood perfusion and metabolism, respectively, and Q is the external source of heat, in our case caused by ultrasound beam radiation. The blood perfusion term is defined as:

$$Q_p(\mathbf{x},t) = \rho_b C_b \omega_b (T_b - T), \quad (2)$$

where ρ_b is the density of blood, C_b is the specific heat of blood, ω_b is a blood perfusion rate, T_b is the arterial blood temperature. In our experiments, performed *in vitro* on TMMs we omitt the perfusion and metabolism terms in Eq. (1), i.e.,:

$$Q_p(\mathbf{x},t) = 0, \qquad Q_{met}(\mathbf{x},t) = 0. \quad (3)$$

Bull. Pol. Acad. Sci. Tech. Sci. 69(3) 2021, e137053

3

The volume V consists of two sub-volumes, $V = V_w \cup V_t$, where V_w denotes the volume occupying by water, and V_t by the tissue, respectively. The coefficients in Eq. (1) are written now as:

$$\rho(\mathbf{x}) = \begin{cases} \rho_w & \text{for } \mathbf{x} \in V_w, \\ \rho_t & \text{for } \mathbf{x} \in V_t, \end{cases} \tag{4}$$

$$C(\mathbf{x}) = \begin{cases} C_w & \text{for } \mathbf{x} \in V_w, \\ C_t & \text{for } \mathbf{x} \in V_t, \end{cases} \tag{5}$$

$$\mathbf{K}(\mathbf{x}) = k(\mathbf{x})\bar{\mathbf{I}}, \qquad k(\mathbf{x}) = \begin{cases} k_w & \text{for } \mathbf{x} \in V_w, \\ k_t & \text{for } \mathbf{x} \in V_t, \end{cases} \tag{6}$$

where $\bar{\mathbf{I}}$ denote the unit second order tensor, lower index t and w standing in the density, specific heat, and the conductivity properties denotes tissue and water medium properties, respectively. To solve the heat transfer equation the temperature on the boundary ∂V of domain V should be determined.

2.3.2. Linear acoustics. In what follows, we remind basic notions of the linear acoustics. Linearized equation of acoustic motion in the fluid medium occupying the region V has the following form

$$\rho \frac{\partial \mathbf{v}(\mathbf{x})}{\partial t} = -\boldsymbol{\nabla} p(\mathbf{x}), \text{ for } \mathbf{x} \in V, \tag{7}$$

where $\rho, \mathbf{v}(\mathbf{x})$ and $p(\mathbf{x})$ denotes medium density, particle velocity and acoustic pressure field, respectively. The constitutive relation coupling the changes in particle velocity and pressure reads as:

$$\frac{\partial p}{\partial t} = -\kappa \boldsymbol{\nabla} \cdot \mathbf{v}, \tag{8}$$

where κ denotes the medium compressibility coefficient. For the case of cylindrical coordinates divergence operator in coordinates (r, θ, z) of vector $\mathbf{a} \equiv (a_r, a_\theta, a_z)$ reads as:

$$\boldsymbol{\nabla} \cdot \mathbf{a} \equiv \frac{1}{r} \frac{\partial}{\partial r}(r a_r) + \frac{1}{r} \frac{\partial}{\partial \theta} a_\theta + \frac{\partial}{\partial z} a_z. \tag{9}$$

In the case of cylindrical symmetry when $\mathbf{a}$ does not dependent on θ Eq. (9) reduces to:

$$\boldsymbol{\nabla} \cdot \mathbf{a} \equiv \frac{1}{r} \frac{\partial}{\partial r}(r a_r) + \frac{\partial}{\partial z} a_z. \tag{10}$$

Based on the assumption of stationarity (harmonic motion), cylindrical symmetry of the sound pressure field generating in our experiment, taking divergence on both sides of Eq. (7), and by using standard manipulation on Eqs. (7)–(9), we get the following homogeneous Helmholtz equation in cylindrical coordinates for pressure field:

$$\frac{\partial}{\partial r}\left[-\frac{r}{\rho_c}\left(\frac{\partial p(r,z)}{\partial r} \right) \right] + r\frac{\partial}{\partial z}\left[-\frac{1}{\rho_c}\left(\frac{\partial p(r,z)}{\partial z} \right) \right]$$
$$- \left[\left(\frac{\omega}{c_c} \right)^2 \right] \frac{r p(r,z)}{\rho_c} = 0, \tag{11}$$

where r and z are the radial and axis coordinates, $p(r,z)$ the acoustic pressure, and ω the angular frequency, respectively. Let us remind that the compressibility coefficient is related to density and speed of sound by the relation $\kappa = \rho c^2$. For the sake of simplicity we assumed that the damping properties of media, in which the wave is propagating, the density ρ_c, and the speed of sound c_c in Eq. (11) are the complex-valued, what is underlined by the addition of lower index c. The standard continuity conditions on the boundary between two sonicated media, water and sample, cf. Fig. 3 are assumed. Additionally, to find the pressure field $p(r,z)$ from Eq. 11 in the finite space domain the proper boundary conditions are formulated below in the subsection *Numerical model*.

The local acoustic intensity field, $\mathbf{I}$, is defined, cf. [38], as a vector field in the direction of the particle velocity, namely:

$$\mathbf{I} = p\mathbf{v}. \tag{12}$$

Intensity of a plane wave propagating in the direction $\mathbf{n}$ reduces to relation:

$$\mathbf{I} \cdot \mathbf{n} = p\mathbf{v} \cdot \mathbf{n}, \qquad I = pv, \tag{13}$$

where the scalars v and I are both being the components in the same propagation direction. Additionally, in the case of plane wave propagating in $\mathbf{n}$ direction acoustic pressure p is related to the scalar particle velocity $v = \mathbf{v} \cdot \mathbf{n}$ by the relation:

$$\rho c v = p, \tag{14}$$

where c is a speed of sound. Substituting Eq. (14) to Eq. (13) we get $I = p^2/\rho c$.

2.4. Ultrasound-thermal coupling. Ultrasound thermal coupling is one-sided here. We do not consider the influence of temperature rise on thermal changes in acoustic wave fields connected to temperature impact on media properties. We restrict only to define the impact of the ultrasound wave propagation on the appearance of heat sources. These sources are directly due to the phenomenon of the ultrasonic absorption, i.e., of transformation a part of ultrasound energy into heat. The ultrasonic wave transmitted from the transducer in the direction of the symmetry axis z, cf. the experimental setup in Fig. 2, losses part of its energy. We assumed that the wave intensity in the axial direction decreases exponentially:

$$I(r,z) = I_0(r,z) \exp^{-2\alpha z}, \tag{15}$$

where $I_0(r,z)$, called initial intensity, is the wave intensity distribution, which would appear in the absence of the tissue, and α is a tissue amplitude attenuation coefficient. If the medium is inhomogeneous on the scale of the wavelength order, or close to it, the wave amplitude decreases as a result of two reasons, acoustic absorption, and scattering. We do not take into account the scattering phenomenon. We assume in what follows that the scattering influence on wave amplitude decrease is much smaller compared to the absorption, so we denote by α, in Eq. 15, the tissue absorption coefficient.

4

Bull. Pol. Acad. Sci. Tech. Sci. 69(3) 2021, e137053

Deposition of thermal energy is associated with the absorption of ultrasonic wave energy in the tissue. The loss of intensity (derivative relative to the variable z along the direction of wave propagation in Eq. (15) determines the amount of heat energy deposited. The following expression, [38], gives the spatially dependent ultrasonic power deposition per unit volume so, the heat source Q from Eq. (1) is defined now as:

$$Q = 2\alpha I = 2\alpha \left| \text{Re}\left(\frac{1}{2}p\mathbf{v}\right) \right|, \tag{16}$$

where α, I, p, $\mathbf{v}$ are the acoustic absorption coefficient, the local acoustic intensity magnitude, the acoustic pressure and acoustic particle velocity vector.

In what follows the acoustic intensity vector $\mathbf{I}$ (SI unit: W/m^2) is defined as the time average, or root mean square (RMS), of the instantaneous energy flow per unit area $p\mathbf{v}$, cf. Eq. (12).

2.5. Specific Absorption Rate, SAR, and thermal dose. An important parameter characterizing the efficiency of hyperthermia is the specific absorption rate, SAR. A comparison of the effect of adding nanoparticles to the tissue to increase the hyperthermia efficiency can be measured by comparing the SAR value of the sample without particles to the SAR value of the sample containing nanoparticles. Determining the SAR from the experimental data requires knowledge of the temperature rise curve in the sample. The SAR is defined as follows:

$$\text{SAR} = C\left(\frac{\mathrm{d}T}{\mathrm{d}t}\right)_{t=0}, \tag{17}$$

where C, [J/(kg·K)] denotes specific heat of tissue, $\left(\frac{\mathrm{d}T}{\mathrm{d}t}\right)_{t=0}$ is a measured initial slope of the heating curve (in the continuum case, a value of the derivative to the curve in the initial time).

The SAR values were calculated using two methods, namely the linear and analytical methods, cf. [39]. In the linear method, we assume that in the first seconds of heating, the thermal conductivity has a negligible effect on the temperature change in the sample, the first term in the right hand side of Eq. (24) is equal 0, and that at the initial moment the temperature increase is equal to 0. So, the heat source power density Q has the following form

$$Q = \rho C \frac{\mathrm{d}T}{\mathrm{d}t}. \tag{18}$$

The solution to Eq. (18) will be a function of $T_{\text{lin}}(t) = At + B$, and the SAR defined in Eq. (17) is estimated as:

$$\text{SAR}_{\text{lin}} = CA. \tag{19}$$

In the analytical method, it is assumed that the ultrasound beam is approximated by the function:

$$Q = 2\alpha I_0 \exp\left(\frac{-r^2}{\beta}\right), \tag{20}$$

where α is the ultrasound absorption coefficient, in units (Np m^{-1}), β is the ultrasound Gaussian variance, in units (m^2), is a measure of beam width.

To use this method, the assumptions are to be met: the beam focus should be in the shape of an ellipse, at least the aspect ratio of the axial to lateral beam width should be greater than two, [39], and the rate of temperature increase across the beam should be much higher than along the beam. Then, the change in temperature over time along the beam axis can be approximated by the function:

$$T(t) = \frac{\overline{C}}{D} \ln(1 + Dt), \tag{21}$$

where parameters $\overline{C} = 2\alpha I_0/\rho C$, $D = 4h/\beta$ and thermal diffusivity $h = k/(\rho C)$. The SAR value, cf.(17), is estimated by:

$$\text{SAR}_{\text{analit}} = C\overline{C}. \tag{22}$$

The goal of hyperthermia in the treatment of malignant tumors is, among others, the direct killing of cells by delivering a suitable thermal dose to the tumor volume. The determination of such a dose was based on an irrefutable experimental fact that maintaining a temperature of 43°C for 240 minutes guarantees irreversible destruction of human cells. The effect of ultrasound on the tissue in the form of a change in its temperature, in any combination of time and temperature, i.e., both during heating and cooling, can be expressed in a number, equivalent to minutes of keeping the tissue at the temperature 43°C. This number, denoted by CEM43°C (cumulative equivalent minutes at 43°C), was introduced in [40] by the following formula:

$$\text{CEM43°C} = \int_{t=0}^{t=t_{\text{final}}} R^{43-T(t)} \, \mathrm{d}t, \tag{23}$$

where $T(t)$ is the time-temperature dependence, $R = 0.5$ above 43°C and $R = 0.25$ below 43°C, interval $(t=0, t=t_{\text{final}})$ is a time interval in which the thermal dose is calculated.

When using local hyperthermia in living tissues, an important issue is to determine the area of the tissue where the tissue undergoes thermal ablation. In these areas, the thermal dose, CEM43°C, must exceed the threshold value of 240 minutes.

2.6. Numerical model. We performed FEM calculations in COMSOL Multiphysics 4.3b software. This required the coupling of the Acoustics Module and the Heat Transfer Module. First, using Acoustics Module we solved the acoustic boundary value problem consisted from the pressure wave equation (11) determined in the whole sonicated domain, cf. Fig. 3.

The boundary conditions for the acoustic pressure equation were given by the four perfectly matched layers (r1, r2, r3, and r4) defined at the edges of the computational domains for absorbing outgoing waves and by the transducer face harmonic displacement. The displacement vibrated with the frequency 5 MHz and had the four different amplitudes corresponding to the four transmitted powers, see Table 2. The transducer was

Bull. Pol. Acad. Sci. Tech. Sci. 69(3) 2021, e137053
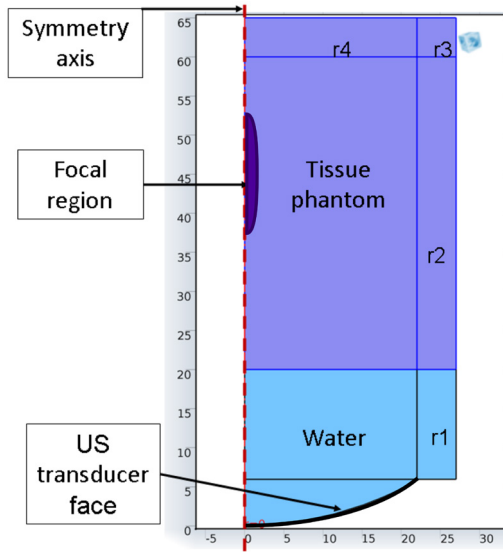
5

B. Gambin and E. Kruglenko

Fig. 3. Geometric diagram assumed in the Comsol model. Four perfectly matched layers r1–r4 are used to absorb the outgoing waves

turned on 5 minutes for sonication and then turned off for cooling. Using the relation (11), we got the distribution of heat sources forcing heat transfer in the sample domain, see Eq. (1). We solved it using the Heat Transfer Module with the Dirichlet boundary conditions, i.e.the medium surfaces were considered to be fixed at the initial temperature of 20°C. So, the sound pressure simulations were performed in both, water and the sample domain, whereas the temperature field simulations were restricted only to the sample domain.

Table 2
Displacement amplitude of transducer (m)

Power	1 W	2 W	3 W	4 W
d	9.2189e–10	1.3037e–09	1.5968e–09	1.8438e–09

A displacement amplitude of transducer for different sound power, from 1 W to 4 W, were given in Table 2. They were calculated from the formula:

$$d = \frac{\sqrt{2I\rho c}}{\rho c \omega}, \qquad (24)$$

where I [W/m^2], ρ [kg/m^3], c [m/s] and ω [rad/s] denoted acoustic intensity, density, speed of sound in water, and transducer circular frequency, respectively. The acoustic intensity was determined from the following formula:

$$I = \frac{P}{S},$$

where P [W] was the measured acoustic power, $S = 0.0017$ [m^2] was surface area of the transducer.

The acoustic and thermal properties of the materials used in the FEM simulation are listed in Table 1. In the meshing of the acoustic model, free triangular mesh elements with the

size of $\lambda/6$, where λ is wavelength, was selected in the focal region and the mesh element in the other regions of the phantom domain had size of $\lambda/4$, while the maximum element size was limited to 0.68 mm. In the perfectly matched layers area the mesh element had the size of 0.2 mm. Quartic (4th order) elements are used to discretize the acoustic pressure, and quadratic (2nd order) elements are used to discretize temperature, see [38].

3. Results

3.1. Beam size estimation. A magnitude of the sound pressure on the beam axis was measured precisely at intervals of 1 mm and 0.25 mm along and across the beam axis, respectively. Figure 4 compares the distribution of measured and numerically determined pressure distributions along and across the beam axis. Based on these results, calculating the value of full width at half maximum (FWHM) pressure amplitude. The size of the focus was determined from FWHM as 1×7 mm. The temperature was measured using seven TP-201 thermocouples (Czaki Termo-Product, Raszyn, Poland) and a USB-TEMP (Measurement Computing) module that recorded the temperature rise over time. The thermocouples located in the sample were located along the beam axis of the heating transducer at intervals of 5 mm at a distance of 5 mm to 35 mm from the border of the sample with water from the side of the transducer transmitting the beam.
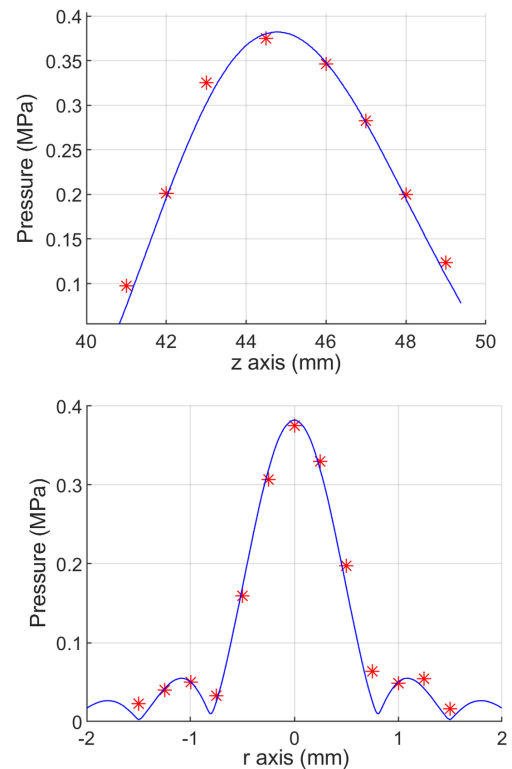

Fig. 4. Comparison of normalized pressure amplitude in the water along the beam axis, z-axis, and across the beam axis, r-axis, the red stars denoted data experimentally determined, and continuous lines were calculated in the acoustic module of FEM, respectively

6

Bull. Pol. Acad. Sci. Tech. Sci. 69(3) 2021, e137053

3.2. Temperature monitoring. The thermocouples positioning along the beam axis enabled to determine the focus position and to follow the temperature rise during the time of sonication in seven points along the beam. In Fig. 5, by adopting the data published in [28], the temperature rise during the first 15 s of ultrasonic heating of the samples for an acoustic power from 1 W to 4 W at the point corresponding to the focus position of the beam, namely, located inside the sample, at a distance of 25 mm from the water – sample border (corresponding to a distance of 45 mm from the transmitter surface) was depicted.

In Table 3 and Table 4 the results of temperature measurements using thermocouples after 15 s and 60 s, respectively, of ultrasound irradiation in the tested samples at the beam focus are presented, i.e., at a distance of 45 mm from the transmitter. When using higher powers, the temperature increase increased accordingly. The highest value of temperature increase, 7.86°C during the first 15 s was observed in MNP16, a sample with a higher content of nanoparticles using a 4 W sound power. The least temperature increase was in a sample made of pure agar. The temperature rise along the beam axis was shown in Fig. 6a
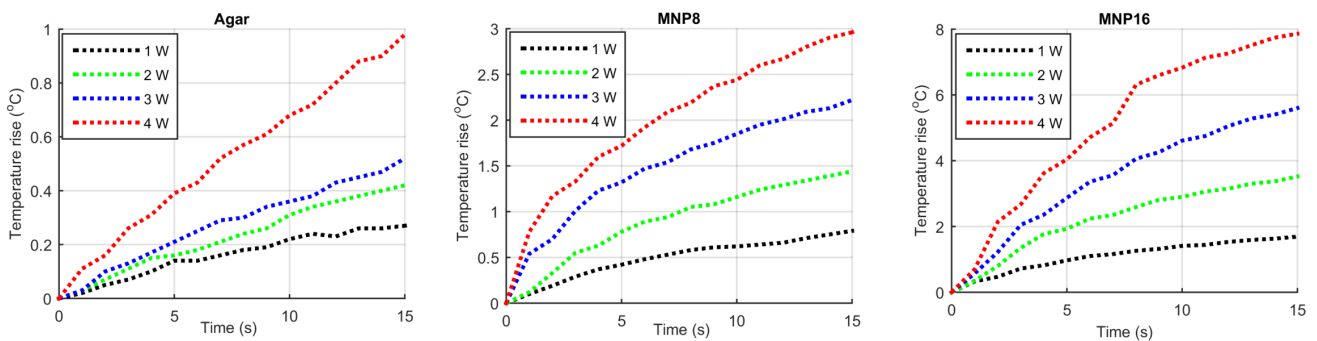

Fig. 5. Temperature rise vs. time during 15 s of experiment measured in the beam focus in Agar, MNP8 and MNP16 samples for four different acoustical power 1–4 W
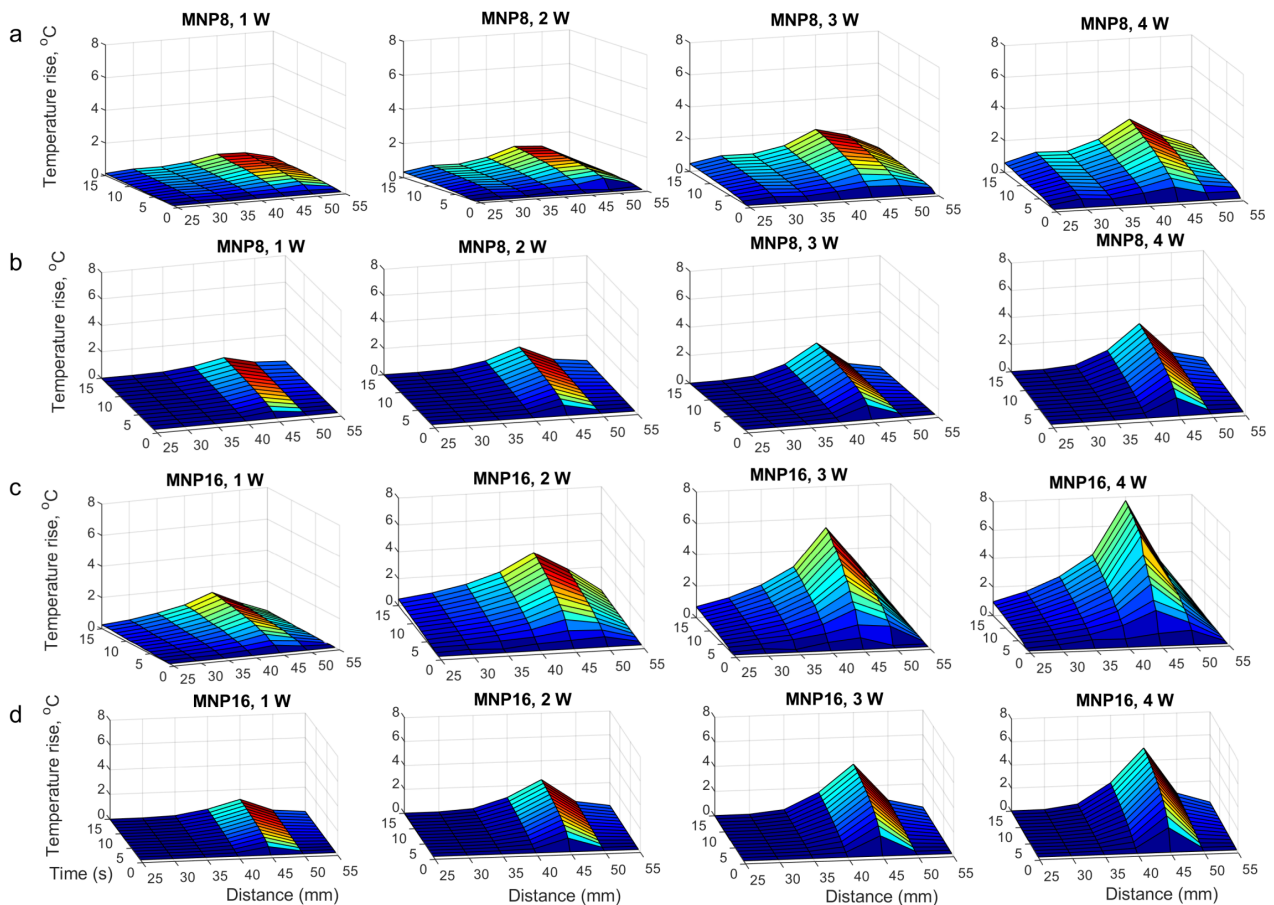

Fig. 6. Temperature rise in the first 15 s at seven points located along the beam axis: "a" and "c" measured by thermocouples, while "b" and "d" obtained by the FEM numerical model

Bull. Pol. Acad. Sci. Tech. Sci. 69(3) 2021, e137053

7

B. Gambin and E. Kruglenko

and Fig. 6c inside MNP8 and MNP16 caused by 4 different acoustic powers by adopting the data published in [28]. The sonication time was limited to the first 15 seconds, and temperature rise curves were measured by seven thermocouples located along the beam axis near the beam focus. All seven thermocouples measurements were used and temperature rise curves are depicted in the seven points laying on the beam axis. Numerically obtained temperature rise curves were calculated in the positions respective to thermocouple positions to illustrate the agreement of time changing of the beam temperature profile, along the beam axis, in the model and experiments.

Table 3

Maximum temperature increases (in °C) in samples for different acoustic powers after 15 s of ultrasonic heating measured with thermocouples

sample	1 W	2 W	3 W	4 W
Agar	0.27	0.42	0.52	0.98
MNP8	0.75	1.39	2.13	2.90
MNP16	1.69	3.52	5.60	7.86

Table 4

Maximum temperature increases (in °C) in samples after 60 s of heating with ultrasound of different powers measured with thermocouples

sample	1 W	2 W	3 W	4 W
Agar	1.04	1.51	2.14	2.40
MNP8	1.29	2.57	3.86	5.06
MNP16	2.82	5.89	8.90	13.01

3.3. Numerical results. Temperature rise curves. To illustrate the acoustic-thermal coupling in FEM calculations, Fig. 7

showed an example solution to the problem of ultrasonic hyperthermia. To the left of this figure, the distribution of the sound pressure field throughout the entire system was shown, including an ultrasonic transmitter, a water layer, and a sample. In this example, it was sample MNP16. The maximum sound pressure, 1.37 MPa, was in the beam focus, 44 mm from the transmitter. On the right side of the figure, the temperature field distribution inside the MNP16 sample was shown, which is located 20 mm from the transmitter. The beam focus, visible as the most heated area, was at 44.45 mm from the transmitter surface, at this area, there was also the maximum temperature value of 6.85°C determined after 15 s of sonication with the acoustic power of 4 W.

The temperature rise in samples MNP8 and MNP16, along the beam axis caused by 4 different acoustic powers, calculated by FEM was shown in Fig. 6b and Fig. 6d. The sonication time was limited to the first 15 seconds, and temperature rise curves were presented in the same location along the beam axis as the locations of seven thermocouples in experiments. The increment in temperature was proportional to the acoustic power rise and content of nanoparticles in samples. Figure 6 showed both results, experimental and numerical, to clarify the differences and similarities between experimantal and numerical results.

Figure 8 showed the results of calculating the temperature field for 300 s of heating and 300 s of cooling of the MNP16 sample at irradiation with the acoustic power of 4 W. The temperature distribution in the sample was shown at different times: 1, 5, 15, 60, 300 s and 600 s.

The temperature increase in the medium depends on the heat sources and the medium's properties such as density, specific heat, and thermal conductivity coefficient, cf. Eq. (1). This increase is the most sensitive to variations of thermal conductivity, cf. [41]. Figure 9 showed the curve of temperature/time dependence during ultrasonic irradiation of the MNP16 sam-
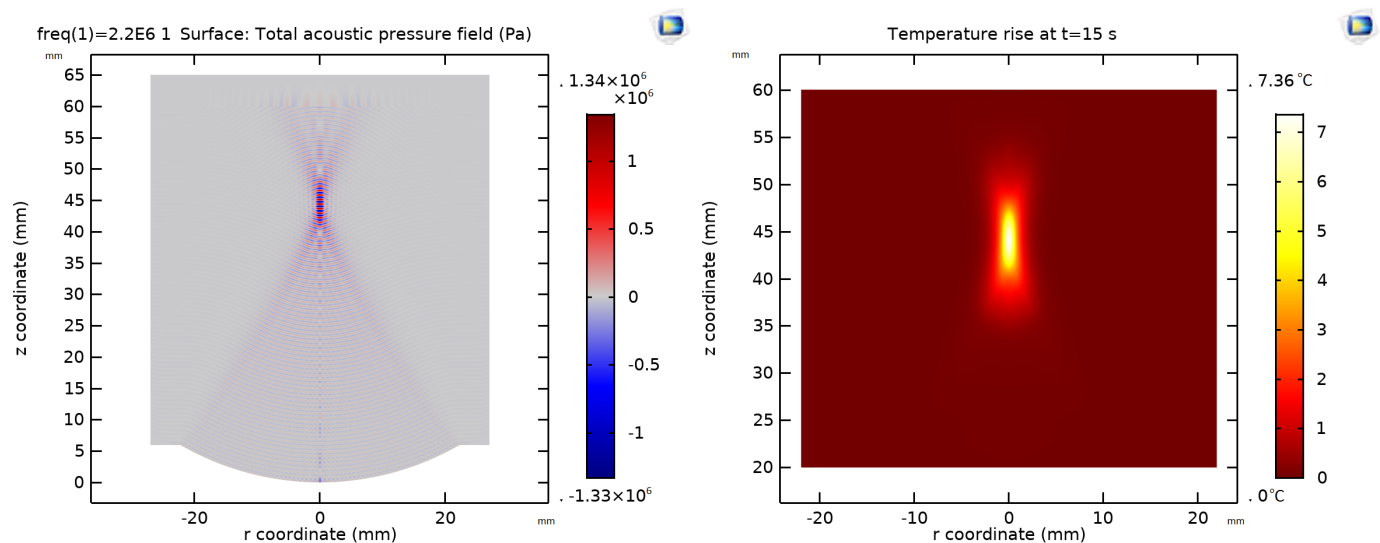

Fig. 7. The results of numerical calculations in the Comsol model: on the left – total acoustic pressure field (Pa) in the sample MNP16, on the right – temperature field distribution after 15 s irradiation with an ultrasonic beam of 4 W sound power
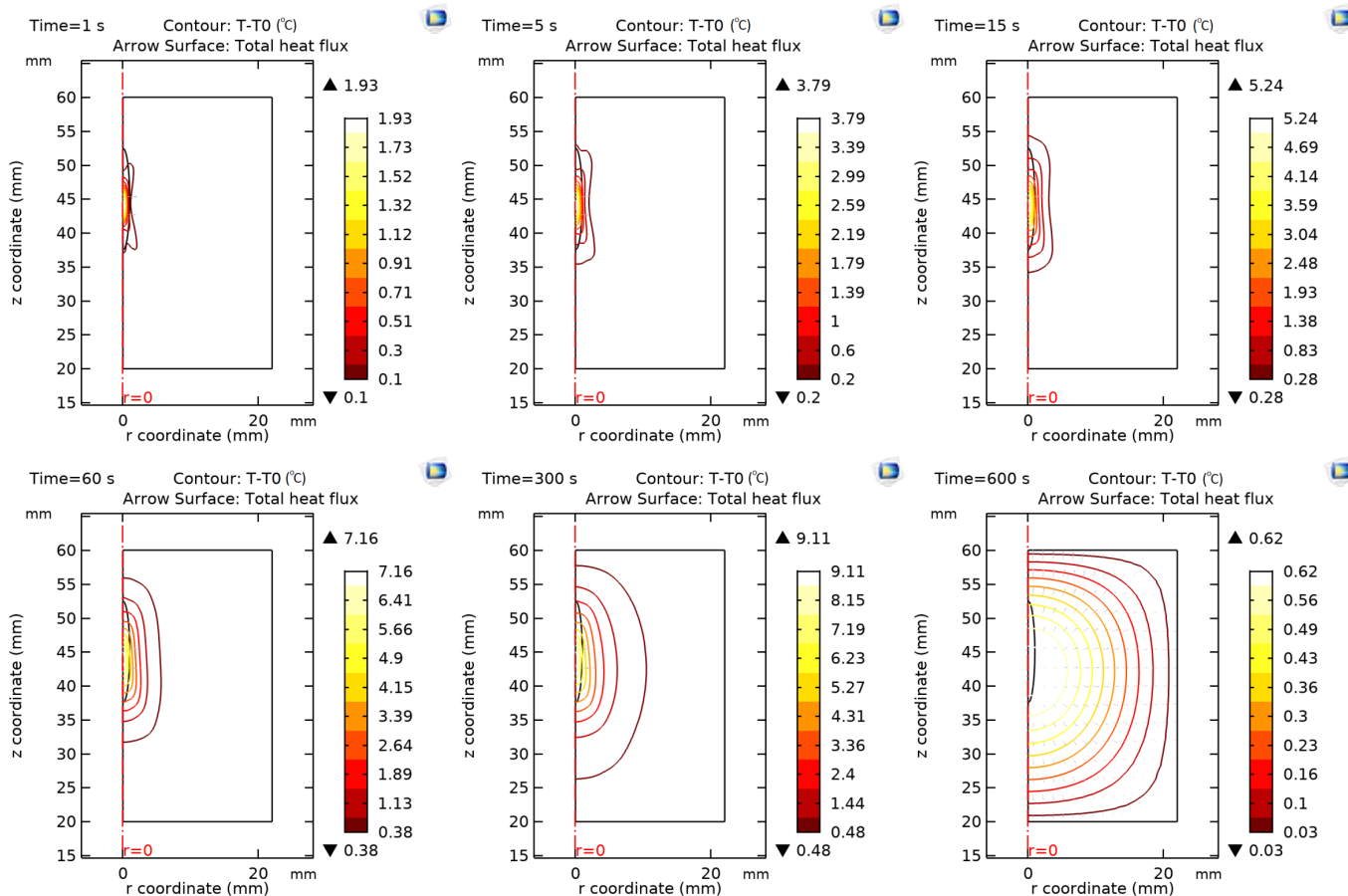
Fig. 8. Temperature distribution in sample MNP16 irradiated with 4 W acoustic power during heating and cooling within 300 s. The temperature distribution in the sample was shown at different times: after 1, 5, 15, 60, 300 s, and 600 s
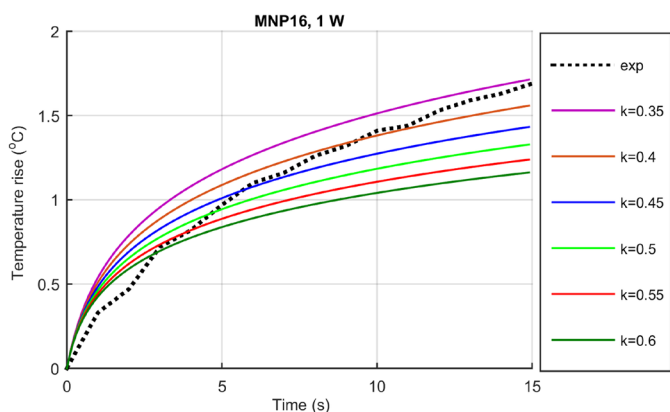

Fig. 9. Comparison of the experimental temperature rise curves, black with the numerical ones for the MNP16 sample at the point of maximum heating, at the acoustic power of 1 W for conductivity values from 0.35 to 0.6 W/(m·K)

ple with a power of 1 W at 15 s, measured with thermocouples and temperature rise curves calculated in Comsol for different values of the thermal conductivity parameter k from 0.35 W/(m·K) up to 0.6 W/(m·K). The argument for using a specific value of thermal conductivity in numerical calculations

was the assessment of the goodness of fit of the temperature increase measured and calculated at the time of sonication less than 15 s.

In Fig. 10 the temperature rise curves in MNP8 samples for two different thermal conductivity of 0.35 and of 0.55 W/(m·K), calculated and measured were presented. Relative distances between the curves "experimental" and "calculated" up to 15 s was 11% and 34% for conductivity, 0.55 W/(m·K) and 0.35 W/(m·K), respectively. After performing such calculation in all cases we decided to use in all numerical calculations discussed in the paper the constant conductivity coefficient of 0.55 W/(m·K).

Let us underline here that all other numerical calculations discussed in the paper were performed with the constant conductivity coefficient, 0.55 W/(m·K).

The comparison of numerical temperature rise curves to experimental ones were used to estimate the sensitivity of the both curves fitting on attenuation coefficient values, see Fig. 11.

Figure 12 compared the temperature increase during the first 30 s of ultrasound irradiation, determined experimentally and calculated in the model (with the same selected heat conductivity coefficient k = 0.55 J/(kg·K)) for all tested samples: agar, MNP8 and MNP16 and acoustic power from 1 W to 4 W.
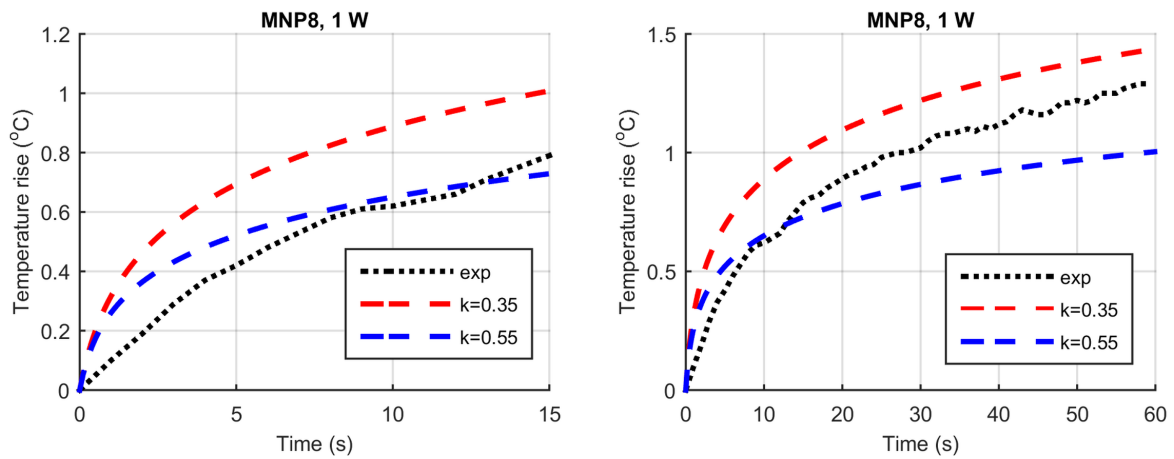
B. Gambin and E. Kruglenko

Fig. 10. Temperature rise vs. time (TvT) curves for sample MNP8 under power of 1 W. TvT curves with red and blue color lines calculated for thermal conductivities of 0.35 W/(m·K), and 0.55 W/(m·K), respectively. The experimental TvT curve has a black color
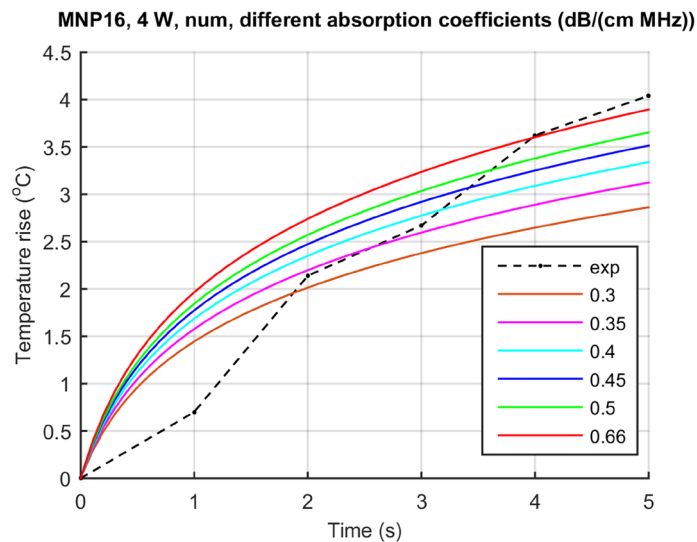
Fig. 11. Comparison of numerical temperature rise curves to experimental one in sample MNP16, heated by acoustic power of 4 W during the first 5 seconds. Attenuation coefficient values changed from 0.3 to 0.66 (dB/(cm·MHz))

Fig. 12. Graphs of temperature changes during 30 s of irradiation, recorded experimentally and calculated in a numerical model for all the tested samples and at different power of the ultrasound beam from 1 W to 4 W. The dotted line corresponds to the experimental result, continuous – numerical result

10

Bull. Pol. Acad. Sci. Tech. Sci. 69(3) 2021, e137053

3.4. Numerical results. SAR and CEM43 estimations.

Figure 13 showed the temperature rise curves in the MNP8 sample for experimental and numerical data together with their linear fitting for the first 5 s of heating, from which the SAR_{lin}, cf. Eq. (19), values for all tested acoustic powers from 1 to 4 W were calculated.
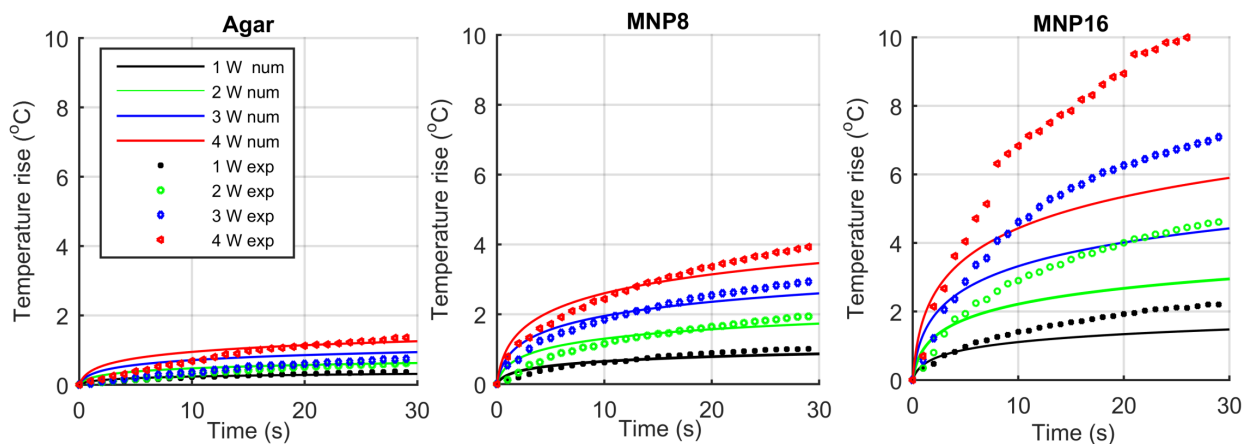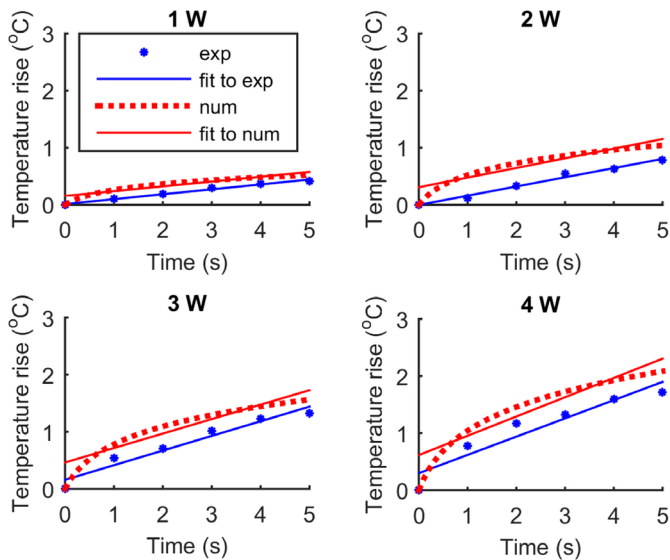

Fig. 13. The graph of temperature increase in the MNP8 sample for experimental, blue doted line, and numerical data, red doted line, and solid line for linear fitting for the first 5 s of heating, blue and red for experimental and calculated data, respectively

Tables 5–7 present the parameters of linear fitting to the temperature rise curves at first 5 s for Agar, MNP8, and MNP16 samples. The value of the tangent to the line equal to the constant A in Tables 5–7 for Agar, MNP8, and MNP16 samples, respectively.

In Fig. 14 the SAR_{lin} dependence on the beam sound power determined from experimental and simulated data for three types of TMMs were presented. Estimation of the linear and quadratic SAR dependence on power values were summarized in Table 8.

Table 5
Fitting parameters of the temperature increase in 5 s to a linear function for the Agar sample

Power	Experimental A	R^2	Numerical A	R^2
1 W	0.02	0.9686	0.05	0.9166
2 W	0.03	0.9927	0.09	0.9165
3 W	0.03	0.9879	0.14	0.9165
4 W	0.06	0.9949'	0.19	0.9165

Table 6
Fitting parameters of the temperature increase in 5 s to a linear function for the MNP8 sample

Power	Experimental A	R^2	Numerical A	R^2
1 W	0.09	0.9904	0.08	0.8971
2 W	0.16	0.9849	0.17	0.8971
3 W	0.26	0.9466	0.25	0.8971
4 W	0.32	0.9177	0.34	0.8971

Table 7
Fitting parameters of the temperature increase in 5 s to a linear function for the MNP16 sample

Power	Experimental A	R^2	Numerical A	R^2
1 W	0.19	0.9704	0.15	0.8981
2 W	0.41	0.9838	0.29	0.8982
3 W	0.59	0.9871	0.44	0.8981
4 W	0.84	0.9770	0.58	0.8981

Tables 9 and 10 presents the fitting parameters of experimental and numerical temperature rise curve in 30 s to logarithmic function given in Eq. (21), used to analytical SAR estimation, SAR_{analit} – cf. Eq. (22), for samples MNP8 and MNP16.
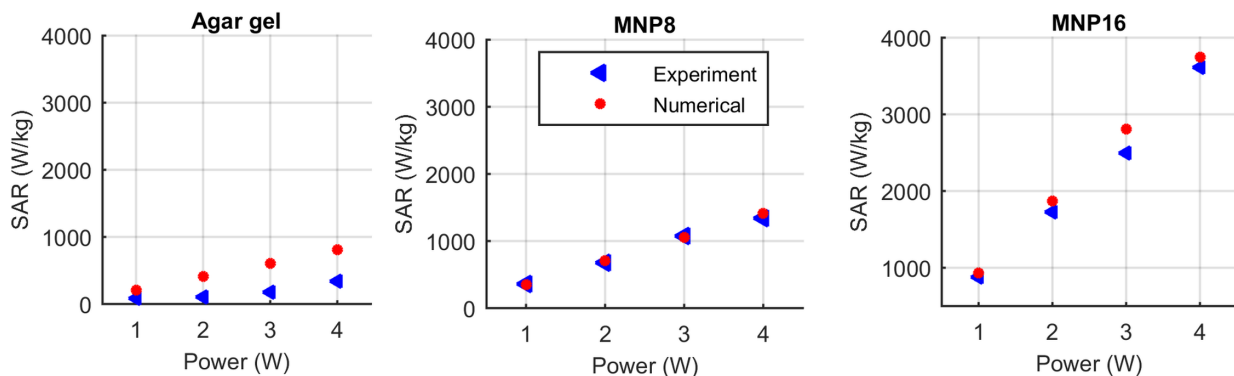

Fig. 14. SAR_{lin} dependence on the beam sound power determined from experimental data and calculated in the numerical model for three types of TMMs

Bull. Pol. Acad. Sci. Tech. Sci. 69(3) 2021, e137053

11

Table 8

Linear and quadratic estimation of SAR dependence on beam power determined from experimental data (exp.) and calculated in the numerical model (num.) for three types of TMMs. $R^2_{\text{lin.exp.}}$ and $R^2_{\text{sq.exp.}}$ denote the error of fitting experimental data to the linear and quadratic function describing the relationship of SAR to the acoustic power of a beam, respectively, and a denotes coefficient in the linear fitting $y = ax + b$

Sample	$R^2_{\text{lin.exp.}}$	$R^2_{\text{sq.exp.}}$	a exp.	a num.
Agar	0.8742	0.9987	83	203
MNP8	0.9950	0.9960	330	353
MNP16	0.9935	0.9979	899	935

Table 9

Fitting parameters of experimental and numerical temperature rise curve in 15 s to logarithmic function, used in estimation of SAR$_{analit}$ for MNP8 sample, where R^2 is coefficient of determination

Power	Experimental $\overline{C}$	D	R^2	Numerical $\overline{C}$	D	R^2
1 W	0.14	0.31	0.9973	0.56	3.01	1
2 W	0.23	0.25	0.9866	1.13	3.01	1
3 W	0.59	0.65	0.9894	1.70	3.01	1
4 W	0.87	0.74	0.9975	2.25	3.01	1

Table 10

Fitting parameters of experimental and numerical temperature rise curve in 15 s to logarithmic function, used in estimation of SAR$_{analit}$ for MNP16 sample

Power	Experimental $\overline{C}$	D	R^2	Numerical $\overline{C}$	D	R^2
1 W	0.36	0.43	0.9983	0.92	2.78	1
2 W	0.63	0.30	0.9938	1.83	2.78	1
3 W	0.83	0.21	0.9971	2.75	2.78	1
4 W	1.28	0.24	0.9892	3.66	2.78	1

In Tables 11–13, the estimated SAR values obtained with the linear and analytical methods were presented for acoustic powers from 1 W to 4 W, based on the experimental and numerical data.

Table 11

SAR (W/kg) for the Agar sample

Power	1 W	2 W	3 W	4 W
Experimental, linear	77	118	139	264
Numerical, linear	195	391	586	782
Numerical, analitycal	871	1740	2610	3481

Table 12

SAR (W/kg) for the MNP8 sample

Power	1 W	2 W	3 W	4 W
Experimental, linear	359	674	1072	1339
Numerical, linear	353	705	1058	1411
Experimental, analitycal	577	963	2501	3616
Numerical, analitycal	2354	4707	7063	9418

Table 13

SAR (W/kg) for the MNP16 sample

Power	1 W	2 W	3 W	4 W
Experimental, linear	877	1724	2449	3615
Numerical, linear	936	1872	2807	3742
Experimental, analitycal	1507	2617	3483	5348
Numerical, analitycal	3821	7643	11460	15277

The following parameters are used to compare the difference in SAR values in the tested samples:

$$S1 = \frac{\text{SAR}_{\text{MNP8}} - \text{SAR}_{\text{agar}}}{\text{SAR}_{\text{agar}}}, \quad (25)$$

$$S2 = \frac{\text{SAR}_{\text{MNP16}} - \text{SAR}_{\text{agar}}}{\text{SAR}_{\text{agar}}}, \quad (26)$$

$$S3 = \frac{\text{SAR}_{\text{MNP16}} - \text{SAR}_{\text{MNP8}}}{\text{SAR}_{\text{MNP8}}}, \quad (27)$$

where lower indices unequivocally denote the sample type for which the SAR was determined.

Table 14

Values $S1$, $S2$, $S3$ defined in Eqs. (25–27), calculated for the linear method

Power	1 W	2 W	3 W	4 W
Experimental, linear $S1$	3.6	4.7	6.7	4.8
Experimental, linear $S2$	10.4	13.6	16.6	13.3
Experimental, linear $S3$	1.4	1.6	1.7	1.7
Numerical, linear $S1$	0.81	0.8	0.81	0.81
Numerical, linear $S2$	2.12	2.12	2.12	2.12
Numerical, linear $S3$	0.73	0.73	0.73	0.73

To calculate the thermal dose the temperature variations in MNP8 and MNP16 we used the experimental data announced in the paper [28], when data were recorded by the 300 s of the heating process and 300 s of cooling. The results of the thermal dose calculation were shown in Fig. 15. The CEM43°C values were calculated from Eq. (23). The CEM43°C = 240 minutes, the threshold indicating the cell death was exceeded only in MNP16 samples in the case of 3 and 4 W of heating powers.
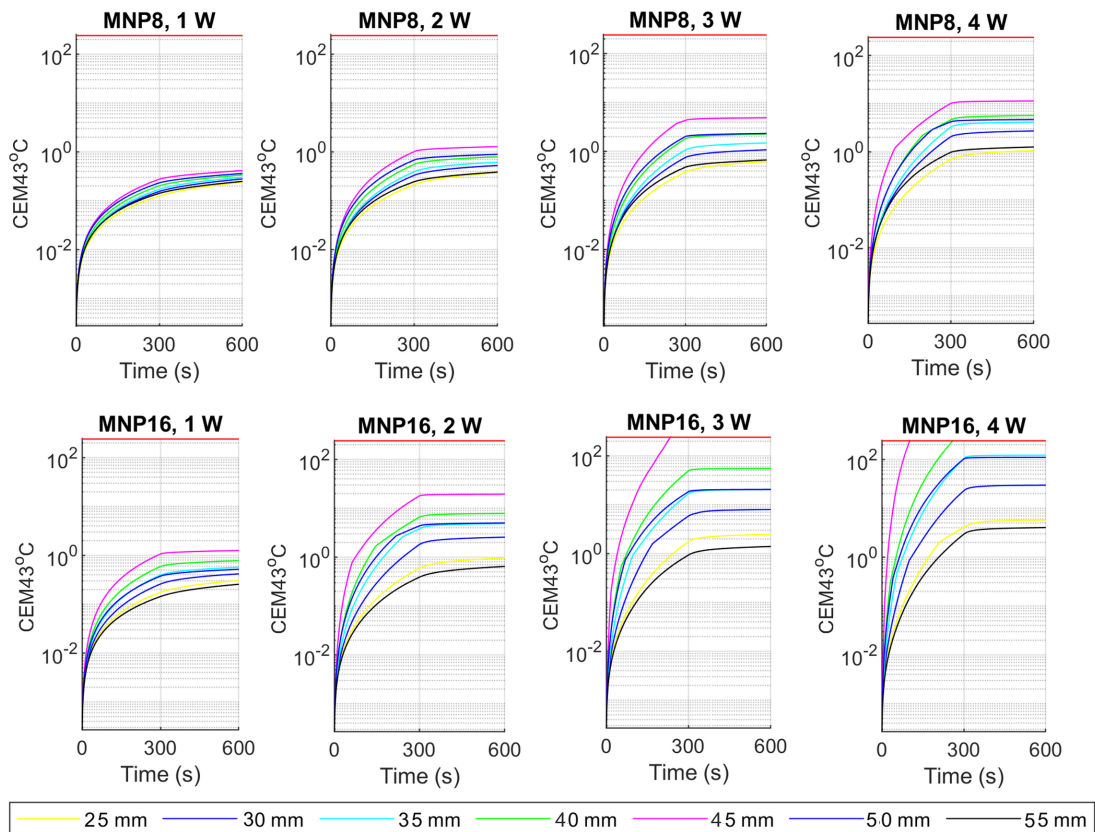
12

Bull. Pol. Acad. Sci. Tech. Sci. 69(3) 2021, e137053

Fig. 15. Temperature variations vs. time, 300 s of heating and 300 s of cooling, presented in log-scale. Experimental data for sample MNP8 and MNP16 for acoustical power of 1-4 W in different distances from the transducer position. Thermal threshold of ablation, red line, equals to CEM43°C

4. Discussion

At first, we confirmed that the measurements and numerical simulation of the beam size in both directions, radial and lateral, in water was a very close one to others, see Fig. 4. Based on this result, we assumed that the distribution of ultrasound pressure inside the samples during the experiments is also correctly estimated. Comparing the temperature rise in the first 15 s measured and simulated along the beam axis at seven points we can conclude that the beam size and its form are sufficiently well numerically simulated, see Fig. 6. The beam focus is 44 mm distant from transducer for samples MNP8 and MNP16 in both graphs, experimentally measured as well as simulated.

The results obtained from the numerical simulation were compared with the experimental results to verify the validity of the numerical model. In agreement with the data presented in Table 3, 4, Fig. 5 and Fig. 12 we summarize below detailed results about temperature rises. For the phantom with MNP8 sample the maximum temperature, registered by thermocouples, raised of 0.79°C, 1.44°C, 2.22°C and 2.96°C after 15 seconds sonication with the acoustic powers of 1, 2, 3 and 4 W, respectively; whereas, the temperature rises, predicted by the numerical simulation, was of 0.73°C, 1.46°C, 2.18°C and 2.92°C, for acoustic powers of 1, 2, 3 and 4 W, respectively. The differences in temperature increments between measurements and

simulations were in the range 0.02–0.07°C, so there were negligibly small. Figure 12 demonstrated that temperature rise was enhanced with the increase of acoustic power and with increasing nanoparticle particle content in samples. In the phantom MNP16 the maximum temperature rise, registered by thermocouples, had value 1.6°C, 3.52°C, 5.6°C and 7.86°C for sonication with acoustic power 1, 2, 3, and 4 W after 15 seconds of sonication, respectively. Meanwhile, the simulated temperature rise was of 1.24°C, 2.48°C, 3.72°C and 4.96°C for sonication with acoustic power 1, 2, 3, and 4 W, respectively. Here, the differences between measurements and simulations were in the range 0.02–2.9°C. The highest discrepancy, which can not be treated as small was in the case of the strongest acoustic power of sonication, 4 W, when the linear acoustic model is not longer enough precise approximation of thermal sources determination in Pennes equation. The maximum temperature increase was recorded – at a distance of 45 mm from the transducer surface, which corresponds to the geometric focus of the beam. Figure 10 showed the experimentally and numerically determined dependencies of the temperature in the MNP8 sample on thermal conductivity values using the acoustic power of 1 W at the point of maximum increase after the first 15 s of exposure to the ultrasound. In the numerical model, the thermal conductivity parameter was changed in the range from 0.35 W/(m·K) to 0.55 W/(m·K). Selecting the thermal conductivity coefficient in

the model so that the temperature values from the calculations are equal to the experimental one, we changed the "numerical" temperature curve: with lower values of the conductivity coefficient, the curve at the beginning grows faster, but the character of the experimental curve is different than the numerical one. The increase of the numerically determined temperature curve over time is much faster at the beginning of heating (5–15 s) than the curve obtained from the experiment, which is in this range more linear. The numerical curves at the beginning of heating are more nonlinear, the conductivity influenced the process from the first seconds, so the rate of temperature increase decreased faster than in the experimental curve. This may indicate that the heating area in the sample is a bit larger and more blurred than that calculated from the numerical model. A similar effect was observed in [24]. This phenomenon was explained by the influence of the delay in temperature reading by thermocouples and the delay in reaching the full acoustic power of electronic devices. From data presented in Figs. 9–10 we concluded that the value of the heat conductivity coefficient did not affect the amount of temperature increase at the very beginning of heating, so on the assessment of the SAR value. For further numerical experiments for agar samples and agar with different amounts of additives, the same value of the thermal conductivity $k = 0.55$ W/(m·K) was selected, while the other physical properties used in numerical simulations there are in Table 1. Conclusions following from the data presented in Fig. 12 we summarize as follows:

- with an increase in the applied sound power from 1 W to 4 W, the temperature in the samples after irradiation, as determined from the experiment, and calculated in the numerical model, grows faster at the beginning and reaches higher values for each sample,
- there was a significant difference in heating the sample from agar alone and agar with the addition of particles, both for the experimental and numerical results. The smallest increase in temperature was obtained for a sample made of agar alone in the range from 0.37°C to 1.36°C for the first 30 s of heating at the heating power of 1–4 W. The temperature increased the most in the agar sample with a higher addition of MNP16 nanoparticles – after 30 s the temperature increase was 10.2°C for the power of 4 W,
- the temperature in the MNP16 sample after 30 seconds of recording was higher than in MNP8 in 2–2.5 times for the same applied powers.
- Agar is less sensitive to heating power than samples with nanoparticles, especially for lower acoustical power used, with the highest acoustic power of 4 W, the rate of temperature rise is the fastest,
- when fitting the numerical results to the experimental results, it is important to define the time interval in which the temperature values for these values are equal. For the used acoustic powers from 1 W to 4 W (and the parameters used in the numerical model), these are time intervals that are successively smaller with the addition of a greater number of nanoparticles, namely for Agar sample, the interval was 10 s – 30 s of heating, MNP8 sample, 10 s–15 s, and MNP16 sample, 3 s–5 s, respectively,

- the length of time for each fit also affects SAR estimation accuracy [40]. The time of the first 5 s was chosen as the length of the fitting of the function to the temperature data for the determination of SAR.

Generally, both the numerical simulation and the experiments produced the similar trends in all presented diagrams. Secondly, both results show that the temperature rise during HIFU was enhanced by increasing the MNP concentration as well as by amplifying the ultrasound acoustic power. Let us remind that in [26] global ultrasonic wave attenuation divided into attenuation due to scattering and absorption in TMMs, which were studied above, namely smaples of Agar, MNP8, and MNP16 were estimated. Based on the assumption that the attenuation coefficient determined experimentally could be divided into two parts:

$$\alpha = \alpha_{\text{absorption}} + \alpha_{\text{scattering}},$$

where $\alpha_{absorption}$ denotes attenuation due to absorption, and $\alpha_{scattering}$ attenuation due to scattering, there was concluded that the attenuation due to absorption in the samples with embedded nanoparticles was dominated. So in our numerical modeling performed here, we assumed the absorption values equal to the measured attenuation values. We do not discuss details of physical background of the absorption phenomena. It is still an open and actual problem, see [24, 25].

It can be seen that the linear estimation of SAR dependence on the acoustic power was well approximated from experimental and simulated data, specially good for samples containing nanoparticles, see Fig. 13 and Tables 5, 6 and 7. The relative error in the linear estimation of the SAR increases depending on power, measured by changing the angle of the slope, was 6 and 4 % for MNP8 and MNP16, respectively, while $R^2 \approx 0.99$ in both samples, MNP8 and MNP16. Square fit dependence errors were comparable, $R^2 \approx 1.00$. For the agar sample, the linear fitment was subject to a relative error of 145%, with $R^2 \approx 0.87$. Fitting to the quadratic relation was more accurate, $R^2 \approx 1.00$. Only in the Agar sample along with the increasing beam power had a SAR growing non-linearly, cf. Table 8; the difference was greater between experimental and calculated data than in the case of samples containing nanoparticles. This difference in the case of agar sample could be associated with stronger than in the case of MNP8 and MNP16 samples, influence of thermocouples artefacts on the temperature increase, discussed more carefully in [24]. We comment here shortly why we did not take into account the heating due to thermocouple presence inside the samples in our numerical modeling. Let us notice that 5 of the thermocouples were located outside the beam focus and they were used only to define the focal region formation. The thermocouple heating artifacts in these measurements were surely negligible. Only two of them were located inside the focal region – one in the center of the focal region, which had the ellipsoidal form with an axis of 0.5 mm and 7 mm, and the second thermocouple was located nearly on the "long end" of an ellipsoid. For this thermocouple, the acoustic intensity was several times smaller than for that located in the central point near the focus. The ends of all the thermocouples lied on the beam axis, and the ther-

14

Bull. Pol. Acad. Sci. Tech. Sci. 69(3) 2021, e137053

mocouples themselves are inserted perpendicular to the axis to minimize artifacts. The thermocouple positioning in the beam focus causes the appearance of an additional heat source, an artifact in the temperature reading. The strongest artifact is due to the "viscous" effect, i.e., the fact that the thermocouple itself is a source of heat, mainly due to the "friction" of environmental molecules against the thermocouple. As it was established in [42] the ratio of a viscous artifact to absorptive heating after 5 s was c/a 0.24 for the thermocouple of the same type as used by us, i.e., for a hypodermic needle thermocouple. The power density of the thermocouple-mediated heat source is restricted to the thin "layer" close to the surface of the volume occupied by the thermocouple sensor contained inside the focal volume, which itself is 3% of the whole beam focus volume. We can conclude that the spatial gradient of the temperature change due to it is locally greater than in the case of acoustic absorption sources distributed over a whole focal volume. So, it can be considered that the influence of the "thermocouple" heat source surely a bit increase the temperature level but mainly this influenced the character of the temperature-versus-time curve, Tvt, character. This effect should be even more pronounced in pure agar samples, where the heat source strength due to absorption is at least of an order of magnitude smaller than in samples doped with nanoparticles. Meanwhile, even for agar samples, the temperature increase in numerical modeling which did not take into account the influence of thermocouples the temperature rise was higher for all powers than the measured, even up to 30 s. The same effect was visible in the first seconds of the measurement for the samples doped with nanoparticles. Taking into account the existence of a thermocouple in the numerical model and another specificity of nanoparticles present in the matrix material would probably allow obtaining a smaller discrepancy between the Tvt curves measured experimentally and obtained from the model. However, the purpose of this work was to evaluate the effect of adding nanoparticles to TMM on the change in absorption. Focusing on analyzing the differences between the results not on finding the strict numerical values of absorption themselves, assuming that we are dealing with linear effects, causes that the artifacts caused by the existence of the thermocouple are significantly eliminated. Moreover, note that the temperature measurements were recorded every 1 second, with an accuracy of 0.5°C, so we used the first 5 seconds of temperature versus time curves to approximate the absorption, not 2–3 seconds. At that time, the measured temperature increase caused by the transmitting power of 4 W was at most 2.5°C for the MNP16 sample. Let us underline that with the transmitting powers from the range of 1–4 W used in our experiments, the intensities of the ultrasonic field in the focus were in the range of 33–132, 27–110, and 15–89 W/cm^2 for the Agar sample, MNP8, and MNP16, respectively. During these first seconds under such low intensities, the thermocouple effect was therefore within reading accuracy and we because of it did not take it into account in our numerical modeling.

The analytical method of SAR estimation was compared to linear estimation in Tables 11, 12 and 13, from which the proportional growth of SAR with power and nanoparticles content

can be recovered. The enhancement of hyperthermia due to the nanoparticle presence measured by SAR calculated from experimental and simulated data was univocally confirmed. Namely, adding a particle fraction of 0.76% w/w to agar increased the SARlinear about 5 times that of pure agar sample from the measured data and about 2 times in the numerical model. Doubling the proportion of nanoparticles, the MNP16 sample, increased the SARlinear about 14 times over pure agar from measured data and about 11 times in the numerical model. An interesting dimensionless measure of the effect of adding nanoparticles on the SAR values is provided in Table 14, in which we compared the relative increases in % of SAR with respect to agar and the comparison of samples MNP8 and MNP16 against each other. Parameter D, see Tables 9–10 and Eq. (21), was the ratio of two parameters, namely thermal conductivity and radial width of the ultrasonic focus. They do not depend on acoustic transmission power. The average value of D was determined from the experimental curves for MNP8 and MNP16 and had a value of 0.489, and 0.295, respectively. Fluctuations in the value of parameter D occurring for the experimental data, Tables 9–10, are the result of the optimization of the temperature-versus-time curve fit to the logarithmic curve allowing for simultaneous changes of both parameters. An interesting result is that the obtained values are of the same order of magnitude as determined from the formula for D, given after (21). The relative difference in D was about 39%. The same tendency to decrease D with a twofold increase in the proportion of nanoparticle content was also observed in the numerical simulations, in which case the analytical method of temperature rise estimation was accurate (matching with $R^2 = 1.00$). The relative difference in the D value was only 8%. Because in the numerical model the thermal conductivity in both samples was assumed to be the same, the 8% difference appeared only due to the sharpening the focus width, because of a much larger medium attenuation coefficient in MNP16 than in MNP8. It follows that a double increase in the doping of agar gel with nanoparticles changes the focus width more strongly because of the appearance of nonlinear effects i.e., the presence of higher harmonics carrying significant acoustic energy absorbed by the medium. It should be studied in the future. We can not compare the results directly to other papers because of differences in sample properties and experimental conditions, but at least one comparison can be done. The SAR values, calculated using the linear method for experimental results in samples with nanoparticles, are of the same order as reported in [33], although the magnetic nanoparticles used in that paper for the production of the samples were an order of magnitude smaller than ours and other ranges of particle content were considered. Indeed, the SAR for the MNP8 sample was by us determined as 674 and 1072 W/kg for 2 and 3 W sound powers, respectively, and in [33] it was 1320 and 2980 W/kg for a constant acoustic power of 2.5 W, but two different frequencies of 1 and 3.5 MHz, while in our study the frequency of 2.2 MHz was fixed. In addition, the SAR values calculated in the same case of MNP8 by us using the analytical method are 1.1–1.7 times greater than those calculated by the linear method, while in [33] they are 5 times greater. At

the end of the discussion, we would like to underline that the CEM43° calculated from experimental data, see Fig. 15 predicted the tissue ablation only in two cases, after 240 s of sonication at 3 W of acoustic power and after 102 s at 4 W, respectively. The numerical simulation did not predict any ablation by the 300 s of sonication and 300 s of cooling in both samples. The numerical simulation did not predict any ablation by the 300 s of sonication and 300 s of cooling in both samples.

5. Conclusions

A comparison of the SAR dependence on increasing acoustic power of ultrasound for agar samples with nanoparticles with calculations in the numerical model confirmed that its usefulness for estimating heating effects in a medium only when its acoustic properties are nearly linear. We proved in this study that the addition of magnetic nanoparticles to tissues significantly increases the value of SAR, and thus increases the efficiency of hyperthermia. Experimental studies were carried out on TMMs made of agar gel with two magnetic nanoparticles fractions of 0.76 and 1.53% w/w. It was shown that SAR increases about agar-gel alone in the mean by 500% and 1400% in samples with the 0.76 and 1.53% w/w of nanoparticle content, respectively. It was also shown that the increase in SAR is proportional to the increase in acoustic power in the range of 1–4 W applied to the transducer of 2.2 MHz. The FEM numerical model of moderate hyperthermia performed in COMSOL Multiphysics, with mimicking the conditions of the experiment, despite the linear propagation and continuous wave assumptions stated, sufficiently quantitatively and qualitatively describe the course of the heating process for the initial 30 seconds. It was demonstrated that both the numerical simulation and the experiments produced similar trends of temperature variations during heating. Both results show that the temperature rise during moderate intensity focused ultrasound was enhanced by increasing the MNP concentration as well as by amplifying the ultrasound acoustic power. But there are significant discrepancies between experimental and numerical results in the prediction of tissue ablation. A local tissue ablation near the beam focus, determined from experimental data, began to form for samples with nanoparticle content of 1.6 mg/ml after 240 secs of sonication at 3 W of acoustic power and after 102 secs at 4 W, respectively. For samples with pure agar gel and fewer nanoparticles content, the ablation did not start even the end of measurements, i.e., during 300 s. Meanwhile, in numerical experiments, the ablation did not start at all, also for MNP16 samples, after 5 minutes of sonication. A tissue ablation in space and time should be estimated in hyperthermia in agreement with the real process. so it is clear that our numerical model cannot be useful for ablation prediction. We need a more sophisticated model of moderate hyperthermia at relatively low acoustic power and frequencies of c/a 2 MHz to predict the ablation. Additional restrictions in hyperthermia planning result from the considered experimental data. The first

limitation of our experimental study is that only two different fractions of the same type of nanoparticles with the same size of 100 nm were considered. Thus, it was possible to attribute differences in heating rate only to nanoparticle fractions in TMMs but not their different sizes or physical properties. A second limitation is that the ultrasonic transducer with one central frequency was used in experiments. To further elucidate the mechanism of nanoparticle-mediated hyperthermia, future studies are warranted to characterize the coupled ultrasonic-thermal effects of the magnetic nanoparticles embedded within TMMs. Knowledge of these thermal mechanisms may facilitate the design optimization of hyperthermia enhancements at the different conditions of sonication. Additionally, in this study only considered homogenous distributions of nanoparticles within tissue-mimicking phantom, which may not be representative of distributions that are achieved *in vivo*. Further investigations are needed to determine heating enhancements feasible with more real nanoparticle distributions in experimental tumors. Summing up, general conclusions are twofold.Firstly, both the numerical simulation and the experiments produced similar results in spatio-temporal temperature field distribution. Secondly, both results of numerical simulations of moderate hyperthermia and measurements with thermocouples show that the temperature rise during moderate intensity focused ultrasound was similarly enhanced by increasing the MNP concentration as well as by amplifying the ultrasound acoustic power. Thirdly, the detailed analyses of SAR values demonstrated precise enough estimation of the temperature field in nanoparticle-mediated moderate hyperthermia by numerical simulations done in COMSOL using the linear ultrasonic wave module. In the end, we conclude, that the usefulness of the numerical modeling of nanoparticle-mediated moderate hyperthermia has been confirmed, and its limitation has been detailed. Additionally we would like to underline that it is well known that particle size plays a great role in nanoparticle mediated hyperthermia efficiency. Larger particles are heated by ultrasound for other reasons than smaller ones. As shown in the work [43], when large particles are present in the gel, the effect of viscous friction of particles prevails, whereas in the gel containing small particles – below 100 microns – the effects of phonon waves prevail. Particle size optimization can be developed due to many factors: the efficiency of hyperthermia itself, the biocompatibility of nanoparticles in living tissue, the ease of sticking to the target in the tissue (to the tumor), the stability of the suspension that is injected into the tissue or circulated, cost and repeatability of manufacturing technology, etc. Since we are interested in focused ultrasound combined with the effect of heating by an alternating magnetic field, the optimization of particle size must take into account the influence of nanoparticle size on the magnetic heating efficiency. Magnetic hyperthermia studies using nanoparticles suggest that the optimal size should be much less than 100 nm. We are currently working on numerical modeling of the phenomenon of heat generation in a gel containing smaller magnetic ones. Our future ultrasonic hyperthermia research will also look at much smaller magnetic nanoparticles, in the c/a 10 nm range.

16

Bull. Pol. Acad. Sci. Tech. Sci. 69(3) 2021, e137053

REFERENCES

[1] E. Ben-Hur, B.V. Bronk, and M.M. Elkind, "Thermally enhanced radiosensitivity of cultured Chinese hamster cells", *Nat. New Biol*. 238, 209–211 (1972).

[2] M.W. Dewhirst, E.J. Ozimek, J. Gross, and T.C. Cetas, "Will hyperthermia conquer the elusive hypoxic cell? Implications of heat effects on tumor and normal-tissue microcirculation", *Radiology* 137(3), 811–817 (1980).

[3] B. Hildebrandt, P. Wust, O. Ahlers, A. Dieing, G. Sreenivasa, T. Kerner, R. Felix, and H. Riess, "The cellular and molecular basis of hyperthermia", *Crit. Rev. Oncol./Hematol*. 43(1), 33–56 (2002).

[4] Z. Izadifar, P. Babyn, and D. Chapman, "Mechanical and Biological Effects of Ultrasound: A Review of Present Knowledge", *Ultrasound Med. Biol*. 43(6), 1085–110 (2017).

[5] A. Mizera and B. Gambin, "Stochastic modeling of the eukaryotic heat shock response", *J. Theor. Biol*. 265, 455–466 (2010).

[6] S.Z. Child, B. Vives, C.W. Fridd, J.D. Hare, C.A. Linke, H.T. Davis, and E.L. Carstensen, "Ultrasonic treatment of tumors— II: Moderate hyperthermia", *Ultrasound Med. Biol*. 6(4), 341–344 (1980).

[7] G. ter Haar, "The Resurgence of Therapeutic Ultrasound – A 21st Century Phenomenon", *Ultrasonics*, 48(4), 233 (2008).

[8] B. Gambin, T. Kujawska, E. Kruglenko, A. Mizera, and A. Nowicki, "Temperature Fields Induced by Low Power Focused Ultrasound in Soft Tissues During Gene Therapy, Numerical Predictions and Experimental Results", *Arch. Acoust*. 34(4), 445–459 (2009).

[9] A. Mizera, and B. Gambin, "Modelling of ultrasound therapeutic heating and numerical study of the dynamics of the induced heat shock response", *Commun. Nonlinear Sci. Numer. Simul*. 16(5), 2342–2349 (2011).

[10] A. Sohail, Z. Ahmad, O.A. Bég, S. Arshad, and L. Sherin, "A review on hyperthermia via nanoparticle-mediated therapy", *Bull. Cancer* 104(5), 452–461 (2017).

[11] S. Taghizadeh V. Alimardani, P.L. Roudbali, Y. Ghasemi, and E. Kaviani, "Gold nanoparticles application in liver cancer", Photodiagnosis Photodyn. Ther. 25, 389–400 (2019).

[12] N.T.K. Thanh, *Magnetic Nanoparticles: From Fabrication to Clinical Applications*, CRC Press, Taylor & Francis, Boca Raton, London, New York, 2012.

[13] S.B. Devarakonda, M.R. Myers, M. Lanier, C Dumoulin, and R.K. Banerjee, "Assessment of gold nanoparticle-mediatedenhanced hyperthermia using mr-guided high-intensity focused ultrasound ablation procedure", *Nano Lett*. 17, 2532–2538 (2017).

[14] S.B. Devarakonda, M.R. Myers, and R.K. Banerjee, "Comparison of Heat transfer enhancement between magnetic and gold nanoparticles during HIFU sonication", *ASME J. Biomech. Eng*. 140, 081003, (2018).

[15] K. Sztandera, M. Gorzkiewicz, and B. Klajnert-Maculewicz, "Gold Nanoparticles in Cancer Treatment", *Mol. Pharm*. 16(1), 1–23 (2019).

[16] S. Sengupta and V.K. Balla, "A review on the use of magnetic fields and ultrasound for non-invasive cancer treatment", *J. Adv. Res*. 14, 97–111 (2018).

[17] P. Das, M. Colombo, and D. Prosperi, "Recent advances in magnetic fluid hyperthermia for cancer therapy", *Colloid Surf. B: Biointerfaces* 174, 42–55 (2019).

[18] N.T.K. Thanh, Clinical Applications of Magnetic Nanoparticle, CRC Press, Taylor & Francis, Boca Raton, London, New York, 2018.

[19] A. Miaskowski, B. Sawicki, and M. Subramanian, "Singledomain nanoparticle magnetic power losses calibrated with calorimetric measurements", *Bull. Pol. Acad. Sci. Tech. Sci*. 66(4), 509–516 (2018).

[20] A. Józefczak, K. Kaczmarek, T. Hornowski, M. Kubovˇcíková, Z. Rozynek, M. Timko, and A. Skumiel, "Magnetic nanoparticles for enhancing the effectiveness of ultrasonic hyperthermia", *Appl. Phys. Lett*. 108(26), 263701 (2016).

[21] K. Kaczmarek, T. Hornowski, R. Bielas, D. Zak, M. Timko, and A. Józefczak, "Dependence of ultrasonic and magnetic hyperthermia on the concentration of magnetic nanoparticles", *Acta Phys. Pol*. A 133, 716–718, (2018).

[22] E. Kruglenko E., M. Krajewski, R. Tymkiewicz, J. Litniewski, and B. Gambin, "Magnetic and ultrasonic thermal effects of magnetic nanoparticles in a tissue phantom", *Applications of Electromagnetics in Modern Techniques and Medicine (PTZE)*, Janow Podlaski, Poland, 2019, pp. 89–92.

[23] K. Kaczmarek, T. Hornowski, I. Antal, M. Rajnak, M. Timko, and A. Józefczak, "Sono-magnetic heating in tumor phantom", *J. Magn. Magn. Mater*. 500, 166396 (2020).

[24] M. Sadeghi-Goughari, S. Jeon, and H. Kwon, "Analytical and Numerical Model of High Intensity Focused Ultrasound Enhanced with Nanoparticles", *IEEE Trans. Biomed. Eng*. (2020).

[25] M. Sadeghi-Goughari, S. Jeon, and H.J. Kwon, "Magnetic nanoparticles-enhanced focused ultrasound heating: size effect, mechanism, and performance analysis", *Nanotechnology* 31(24), 24510 (2020).

[26] B. Gambin, E. Kruglenko, R. Tymkiewicz, and J. Litniewski, "Ultrasound assessment of the conversion of sound energy into heat in tissue phantoms enriched with magnetic micro- and nanoparticles", *Med. Phys*. 46(10), 4361–4370 (2019).

[27] T. Drakos, M. Giannakou, G. Menikou, C. Ioannides, and C. Damianou, "An improved method to estimate ultrasonic absorption in agar-based gel phantom using thermocouples and MR thermometry", Ultrasonics 103, 106089 (2020), doi: 10.1016/j. ultras.2020.106089.

[28] E. Kruglenko, I. Korczak, J. Litniewski, and B. Gambin, "Ultrasound Thermal Effect Enriched by Adding of Micro and Nano Particles to the Agar-Gel Tissue Mimicking Materials", *2018 Joint Conference – Acoustics* Ustka, Poland, 2018, pp. 1–6.

[29] T. Kujawska, W. Secomski, E. Kruglenko, K. Krawczyk, and A. Nowicki, "Determination of Tissue Thermal Conductivity by Measuring and Modeling Temperature Rise Induced in Tissue by Pulsed Focused Ultrasound", *Plos One* 9, e94929 (2014).

[30] J. Lyklema, "The bottom size of colloids", *Bull. Pol. Acad. Sci. Tech. Sci*. 53(4), 317–323 (2005), doi: 10.24425/123928.

[31] P.C. Morais, "From magnetic fluids up to complex biocompatible nanosized magnetic systems", *Bull. Pol. Acad. Sci. Tech. Sci*. 56(3), 253–262 (2008).

[32] M. Zhang, Z. Che, J. Chen, H. Zhao, L. Yang, Z. Zhong, and J. Lu, "Experimental Determination of Thermal Conductivity of Water-Agar Gel at Different Concentrations and Temperatures", *J. Chem. Eng. Data* 56(4), 859–864 (2011).

[33] K. Kaczmarek, T. Hornowski, M. Kubovčíková, M. Timko, M. Koralewski, and A. Józefczak, "Heating Induced by Therapeutic Ultrasound in the Presence of Magnetic Nanoparticles", *ACS Appl. Mater. Interfaces* 10(14), 11554–11564 (2018).

[34] B. Gambin and E. Kruglenko, "Temperature Measurement by Statistical Parameters of Ultrasound Signal Backscattered from Tissue Samples", *Acta Phys. Pol*. 128(3), A72–A7867 (2015).

B. Gambin and E. Kruglenko

[35] P. Karwat, T. Kujawska, P.A. Lewin, W. Secomski, B. Gambin, and J. Litniewski, "Determining temperature distribution in tissue in the focal plane of the high (>100 W/cm^2) intensity focused ultrasound beam using phase shift of ultrasound echoes", *Ultrasonics* 65, 211–219 (2016).

[36] S.C. Brüningk, I. Rivens, P. Mouratidis, and G. Ter Haar, "Focused Ultrasound-Mediated Hyperthermia in Vitro: An Experimental Arrangement for Treating Cells under Tissue-Mimicking Conditions", *Ultrasound Med. Biol.* 45(12), 3290–3297 (2019).

[37] H.H. Pennes, " Analysis of Tissue and Arterial Blood Temperatures in the Resting Human Forearm", *J. Appl. Physiol.* 1(2), 93–122 (1948).

[38] COMSOL Multiphysics 4.3b, application ID: 12659, "Focused Ultrasound Induced Heating in Tissue Phantom" [Online]. Available: https://www.comsol.com/model/focused-ultrasound-induced-heating-in-tissue-phantom-12659.

[39] C.R. Dillon, U. Vyas, A. Payne, D.A. Christensen, and R.B. Roemer, "An analytical solution for improved HIFU SAR estimatOnly in the Agar sampleion", *Phys. Med. Biol.* 57, 4527–4544 (2012).

[40] S.A. Sapareto and W.C. Dewey, "Thermal dose determination in cancer therapy", *Int. J. Radiat. Oncol. Biol. Phys.* 10, 787–800 (1984).

[41] B. Gambin, E. Kruglenko, T. Kujawska, and M. Michajłow, "Modeling of tissues in vivo heating induced by exposure to therapeutic ultrasound", *Acta Phys. Pol. A* 119, 950–956 (2011).

[42] H. Morris, I. Rivens, A. Shaw and and G. ter Haar, "Investigation of the viscous heating artifact arising from the use of thermocouples in a focused ultrasound field", *Phys. Med. Biol.* 53, 4759–4776 (2008).

[43] C. Bera, S. Devaraconda, V. Kumar, A. Ganguli, and R. Banerjee, "The mechanism of nanoparticle-mediated enhanced energy transfer during high-intensity focused ultrasound sonication", *Phys. Chem. Chem. Phys.* 19(29), 19075–19082 (2017).

18

Bull. Pol. Acad. Sci. Tech. Sci. 69(3) 2021, e137053